

Article

Precipitation Behavior of ω_0 Phase in Ti-37.5Al-12.5Nb Alloy

Teng Ye ¹, Lin Song ^{2,*}, Maohua Quan ³, Jianping He ¹ and Junpin Lin ^{1,*}

¹ State Key Laboratory for Advanced Metals and Materials, University of Science and Technology Beijing, Beijing 100083, China; whoisyt@126.com (T.Y.); sem250@ustb.edu.cn (J.H.)

² State Key Laboratory of Solidification Processing, Northwestern Polytechnical University, Xi'an 710072, China

³ Institute for Advanced Materials and Technology, University of Science and Technology Beijing, Beijing 100083, China; mhquan@ustb.edu.cn

* Correspondence: songlin@nwpu.edu.cn (L.S.); linjunpin@ustb.edu.cn (J.L.); Tel.: +86-10-6233-2192 (J.L.); +86-29-8849-1764 (L.S.)

Academic Editor: Tilmann Beck

Received: 27 April 2017; Accepted: 19 May 2017; Published: 26 May 2017

Abstract: Mutual transformation between α_2 and ω_0 phases has been an interesting topic in recent years. In this study, martensitic α_2 was obtained by air-cooling from 1250 °C in Ti-37.5Al-12.5Nb (at%) alloy while four ω_0 variants formed in the β_0 phase matrix during the cooling process. Nonetheless, only one ω_0 variant was observed at the periphery of the α_2 plates in the β_0 phase and the orientation relationship between these two phases was $[0001]_{\alpha_2} // [1\bar{2}10]_{\omega_0}$; $(11\bar{2}0)_{\alpha_2} // (0002)_{\omega_0}$. Thin γ plates precipitated within the α_2 phase and were thought to be related to the appearance of ω_0 phase. The redistribution of the compositions during the phase transformations was studied by energy dispersive X-ray spectroscopy analysis. The corresponding mechanisms of the phase transformations mentioned above are discussed.

Keywords: titanium aluminides; ω_0 phase; TEM; HRTEM

1. Introduction

High Nb-containing TiAl (Nb-TiAl) alloys have been considered as potential materials for high-temperature applications due to their low density, high strength, good oxidation resistance, and creep properties [1–3]. Recently, Stark et al. showed that the amount of ω_0 phase increased with the content of Nb in high Nb-TiAl alloy [4,5]. Meanwhile, Nb is a β phase stabilizer that extends the β phase field and facilitates the ordered ω (ω_0) phase transitions in the β_0 phase in high Nb-TiAl alloys [6–9]. Numerous studies have reported the ω_0 phase transformations in high Nb-TiAl alloys, indicating that the ω_0 phase is stable at 700–900 °C [10,11]. However, these studies have mainly focused on the transition process between the β_0 and ω_0 phases [6–13] or the α_2 to β_0 phase [14–16]. Recently, some reports concentrated on the precipitation of the ω_0 phase in α_2 laths during aging and studied the relationship between the α_2 and ω_0 phases [10,17–20]. To summarize, there are two different thoughts regarding the precipitation of ω_0 from α_2 phase. First, Huang et al. reported the perpendicular decomposition of coarse α_2 laths in Ti-44Al-8Nb-B alloy and suggested that the α_2 to $\beta_0(\omega)$ transformation occurred after exposing at 700 °C in air for up to 10,000 h, indicating the occurrence of $\alpha_2 \rightarrow \beta_0 \rightarrow \omega_0$ transformation [17]. Similar cases of $\alpha \rightarrow \beta \rightarrow \omega$ transformation in titanium alloys had been reported by Vohra et al. [18] and Gupta et al. [19]. Second, Bystrzanowski et al. observed that the applied stress could enhance the ω_0 precipitation and suggested that the ω_0 precipitation was directly transformed from the α_2 phase [20]. Furthermore, Song et al. observed the direct α_2 to ω_0 phase transformation in Ti-45Al-9Nb alloy after aging at 900 °C [10]. Although

these studies discussed the transformation process and orientation relationships (ORs) between the ω_o and α_2 phases, few reports focused on the nucleation sites of the ω_o phase and the preferential ORs between the ω_o and α_2 phases. Moreover, the nucleation behavior of ω_o particles associated with α_2 phase in β_o phase has scarcely been reported. In this work, the precipitation of ω_o phase in Ti-37.5-12.5Nb alloy was examined. The preferential OR between the ω_o and α_2 phases was evaluated. The corresponding mechanisms were also discussed.

2. Materials and Methods

An ingot of the Ti-37.5Al-12.5Nb (at%) used in this study was prepared using induction levitation melting. The ingot was flipped and remelted three times to ensure compositional homogeneity. Table 1 lists the chemical compositions measured via wet chemical analysis. Specimens with sizes of $10 \times 10 \times 10$ mm were cut from the center of the ingot by electric-discharge machining. The specimens were heat treated at 1250 °C for 2 h followed by air cooling with a cooling rate of approximately 20 K/s. The microstructures after heat treatments were examined using a Zeiss Supra 55 scanning electron microscope (SEM) in back-scattered electron (BSE) mode. Thin foils used for transmission electron microscopy (TEM) observation were prepared by twin-jet electro-polishing in a solution of 65 vol% methanol, 30 vol% butanol, and 5 vol% perchloric acid at 30 V and -30 °C. TEM analysis was conducted on a Tecnai G² F30 field emission transmission electron microscope operating at 300 kV. The compositions were obtained by energy dispersive X-ray spectroscopy (EDS) on TEM. Each parameter was an average value of more than five results measured at different locations.

Table 1. Chemical composition of the as-cast material.

Elements	Ti	Al (at%)	Nb (at%)	O (wt%)	N (wt%)
Composition	Bal.	37.0	13.0	0.018	0.0086

3. Results

The actual composition of the alloy is Ti-37.0Al-13.0 Nb, as obtained by chemical analyses, which is close to the nominal composition. Figure 1a shows the BSE image of the Ti-37.5Al-12.5Nb alloy after air-cooling. The microstructure is composed of α_2 plates and β_o matrix which can be identified by TEM as in Figures 1b and 2b. The well-defined dark lines (arrowed in Figure 1a) observed in α_2 plates are believed to be the midribs of the martensite, which is similar to the result for the α_2 phase form from the β phase by iced-brine quenching in Ti-44Al-4Nb-4Hf-0.1Si [21]. It is difficult to distinguish whether the ω_o phase exists in the β_o region or not from the SEM image. Thus, the precipitation behavior of the ω_o phase can be studied by using TEM. Figure 1b shows the bright-field TEM image of the air-cooled sample. Some particles with sizes of tens of nanometers distribute uniformly in the β_o region. The corresponding selected area diffraction (SAD) pattern of the β_o region is shown in Figure 1c, indicating that β_o phase can readily transform to ω_o phase during air cooling in this alloy.

Commonly, the observed ω_o phase in high Nb-TiAl alloys can form from the “ ω -collapse” in β_o phase [6], i.e., the {111} β_o layers “collapse” and the “-A-B-A-B-A-B-A-” stacking sequence in β_o phase transforms into “-A-B/A-B-A/B-A-”. There are four equivalent {111} β_o layers so that four possible ω_o variants can form in one β_o grain. Considering the ORs between these four ω_o variants and β_o phase, the {01 $\bar{1}$ 0} ω_o diffraction spots of two ω_o variants (denoted as “ ω_{o1} ” and “ ω_{o2} ” in Figure 1c) can be observed at $1/3\{112\}$ β_o under the zone axes: $\langle 110 \rangle_{\beta_o} / \langle 2\bar{1}\bar{1}0 \rangle_{\omega_{o1}}, \omega_{o2}$. However, the $\langle 01\bar{1}2 \rangle$ zone axes of “ ω_{o3} ” and “ ω_{o4} ” are parallel with $\langle 110 \rangle_{\beta_o}$ thus the diffraction patterns of these zone axes are overlapped completely. As a result, the intensities of the superposition spots of the ω_o and β_o phases are significantly increased in Figure 1c.

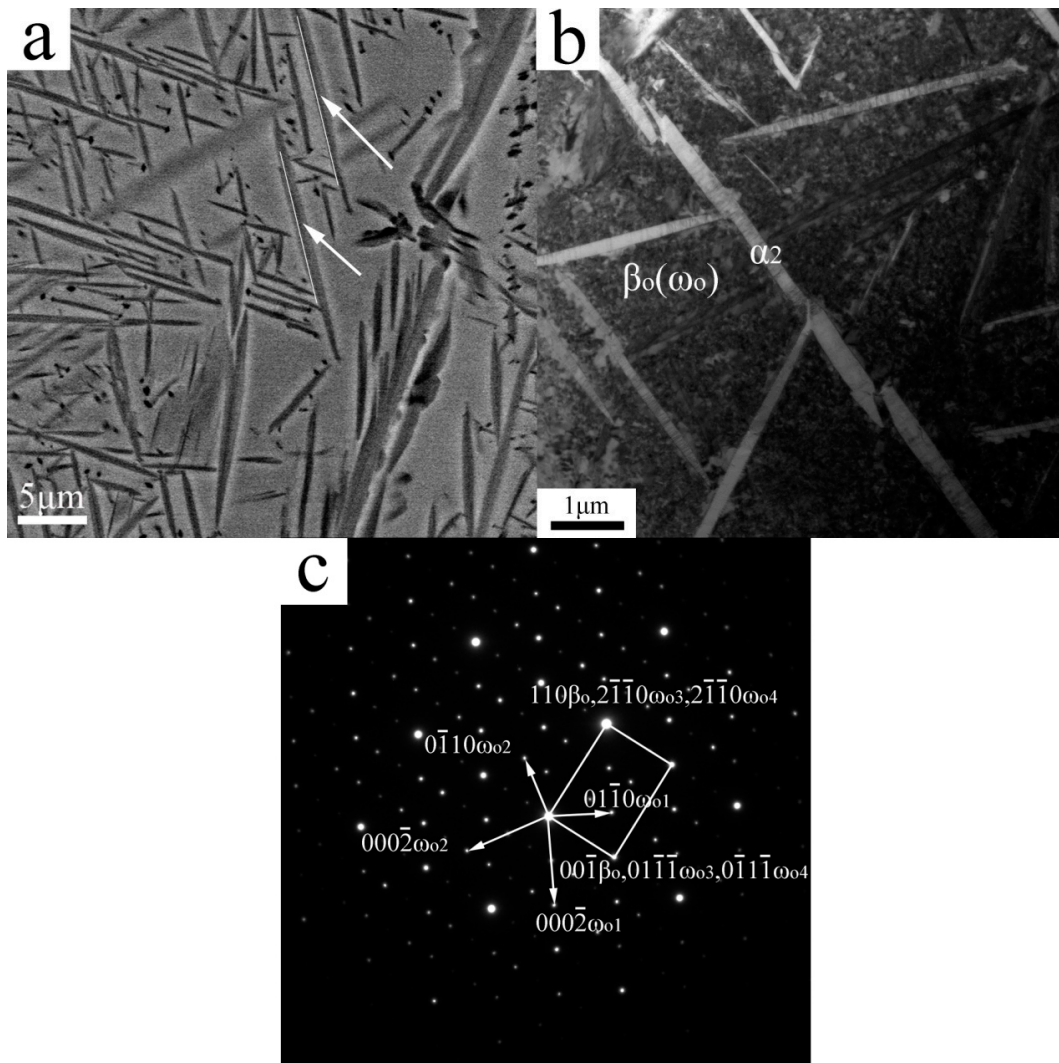


Figure 1. Microstructure of the Ti-37.5Al-12.5Nb alloy after annealing at 1250 °C for 2 h followed by air cooling: (a) back-scattered electron (BSE) image; (b) bright-field transmission electron microscopy (TEM) image; (c) the corresponding selected area diffraction (SAD) pattern of the β_0 region in (b).

Figure 2a shows the bright-field image of the α_2 plates. The circled area in Figure 2a demonstrates an almost precipitate-free region except for some particles that precipitate at the boundary of the α_2 phase. The corresponding SAD pattern of this area is shown in Figure 2b. Only one $\{01\bar{1}0\}$ ω_0 spot exists at $1/3\{112\}$ β_0 under the same beam direction as Figure 1c, which indicates that only one ω_0 variant exists at the α_2/β_0 boundary. The OR between these phases is obtained as:

$$[110] \beta_0 // [0001] \alpha_2 // [1\bar{2}10] \omega_0; (\bar{1}\bar{1}1) \beta_0 // (11\bar{2}0) \alpha_2 // (0002) \omega_0$$

Figure 2c is the corresponding dark field image taken by using the diffraction spot of the ω_0 variant, as circled in the SAD pattern in Figure 2b. It is indicated that the precipitates at the α_2/β_0 boundary are of one kind of ω_0 variants. The compositions of the different phases (denoted in Figure 2a) were obtained by EDS equipped on TEM in Table 2. The results show that the ω_0 precipitates at the periphery of the α_2 phase are more concentrated in Nb than β_0 -matrix and α_2 phase. This case can be interpreted in that Nb is a stabilizing element of the ω_0 phase rather than of the β_0 and α_2 phases [22–24]. Thus, ω_0 precipitations at the α_2/β_0 boundary are more concentrated in Nb than β_0 and α_2 phases because of the expulsion of Nb in the β_0 and α_2 phases during the cooling process.

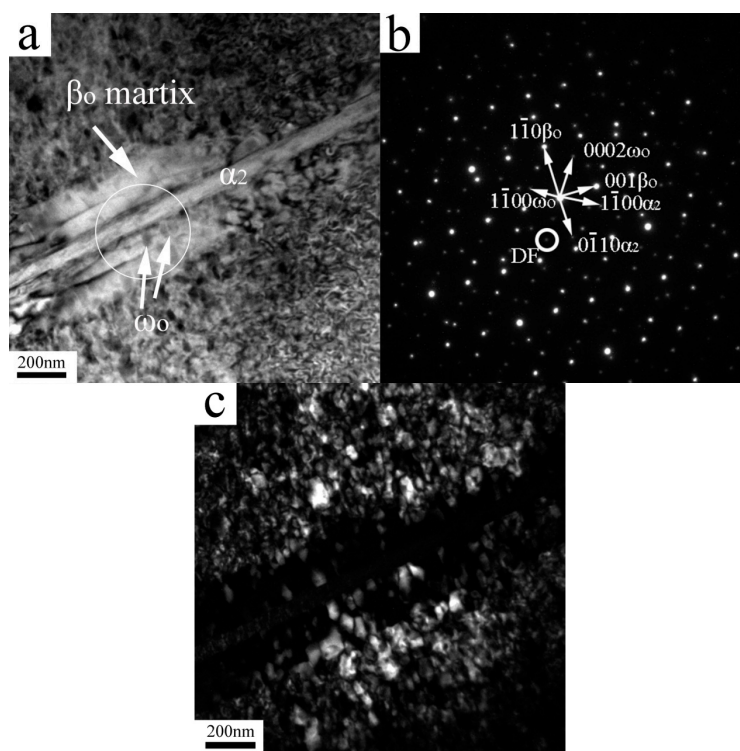


Figure 2. TEM images of (a) bright-field image of the α_2/β_0 boundary; (b) the corresponding SAD pattern at the α_2/β_0 boundary; (c) dark-field image of the same area obtained by taking the spot of the ω_0 phase circled in the SAD pattern in (b).

Table 2. Energy dispersive X-ray spectroscopy (EDS) results of different phases.

Regions	Composition (at %)		
	Ti	Al	Nb
β_0 martix	49.9 ± 0.8	38.5 ± 0.5	11.6 ± 0.8
ω_0	49.5 ± 0.7	36.7 ± 0.5	13.8 ± 0.8
α_2 plate	51.1 ± 0.8	38.1 ± 0.5	10.8 ± 0.8

Figure 3 shows the High-resolution TEM (HRTEM) image of the α_2/β_0 interface obtained under $[0001]_{\alpha_2}$ direction. The fast Fourier transformation (FFT) images of the ω_0 and β_0 areas are shown in Figure 3b,c respectively. It is demonstrated that ω_0 phases sized about a few tens of nanometers nucleate at the α_2 boundary in Figure 3a. This indicates that the preferential ω_0 phase can nucleate at the boundary of α_2 phase and keep a certain OR with α_2 phase.

Further studies on the interior of the α_2 phase reveal that there are a few stacking faults in it. Figure 4a shows some fine-scale planar defects within the α_2 phase, indicating certain phase transformations occur, as also suggested by the distortions at the boundary of the α_2 plate. Figure 4b is the HRTEM image of the interface between the α_2 and β_0 phase. The β_0 region and an ω_0 precipitate nucleated at the α_2 boundary are observed (the corresponding FFT images are shown in Figure 4c,d). It is worth pointing out that although the beam direction is $[11\bar{2}0]_{\alpha_2}$ and the ω_0 precipitate is under $[0001]_{\omega_0}$ direction, the OR between these two phases is as same as those obtained in Figures 2 and 3. The magnified image of Figure 4b is shown in Figure 4e, the atomic stacking sequence of the α_2 phase changes from “-ABAB-” to “-ABCABC-” (FCC-stacking) due to Shockley partial dislocations moving on alternate basal plane (0001) α_2 planes. Repeating this mechanism every two basal planes of the hexagonal matrix leads to the crystal structure change, thus, the stacking faults can act as the nucleus of the γ phase [25,26]. Moreover, it has also been reported that γ phase precipitated in this alloy

after annealing at 700 °C for 26 days [6]. However, the γ phase observed in [6] consists of γ grains precipitated directly from the matrix and not thin γ laths transformed from the α_2 phase. Despite the different morphologies, these facts suggest that the γ phase is an equilibrium phase.

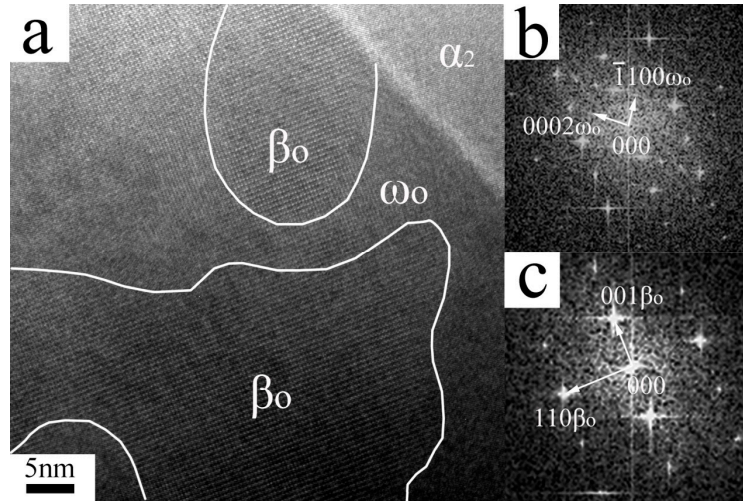


Figure 3. (a) High resolution TEM (HRTEM) image of the α_2/β_0 interface, the corresponding fast Fourier transformation (FFT) images of ω_0 and β_0 areas denoted in (a) are shown in (b,c) respectively.

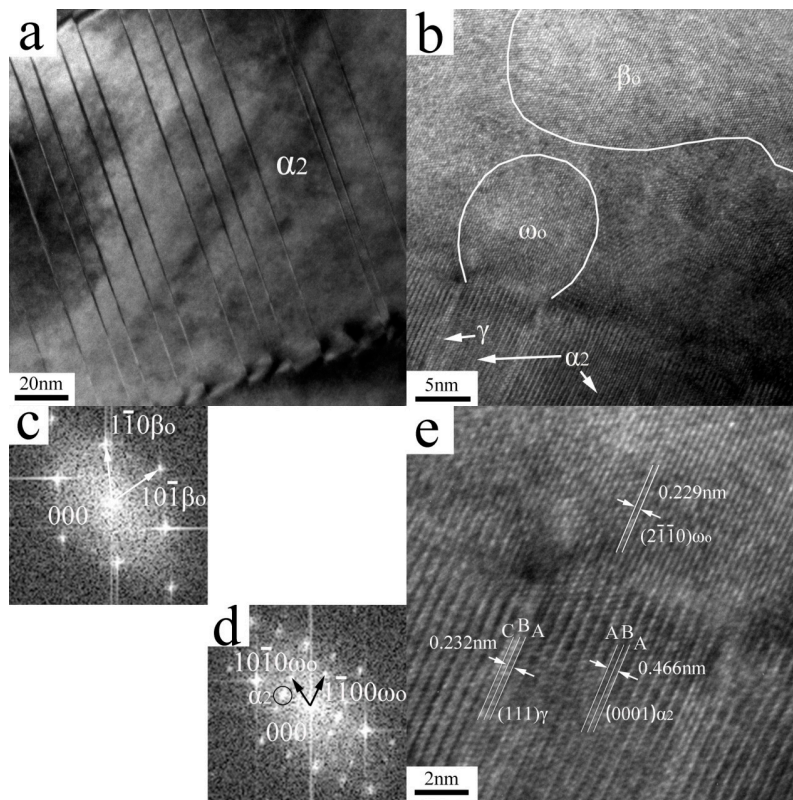


Figure 4. (a) TEM image of the α_2 plate; (b) HRTEM image of the α_2 boundary; (c,d) the corresponding FFT images transformed from the ω_0 and β_0 regions in (b); (e) the magnified image of (b) at the α_2/ω_0 interface.

4. Discussion

4.1. Single ω_o Variant Nucleated at the α_2 Boundary

Transformation matrices are useful for calculating the ORs between the precipitation and matrix phase, which has been widely used in calculating the habit-planes and misorientations [27–30]. As described above, four possible ω_o variants exist in the β_o phase. The ORs between the ω_o variants and β_o phase and between the ω_o and α_2 phases are calculated by using the transformation matrices. The transformation matrices **B** for β_o to ω_o phases are shown in Table 3 (see Appendix A.1 for details). According to the Burgers OR between the α_2 and β_o phases: $\{110\} \beta_o // (0001) \alpha_2$; $\langle 1\bar{1}1 \rangle \beta_o // \langle 11\bar{2}0 \rangle \alpha_2$, six β_o variants can form from the α_2 phase and the transformation matrices **C** for these variants are shown in Table 4 (see Appendix A.2 for details). The hypothesis is that the ORs between the α_2 and ω_o phases can be transferred by the relationships between α_2 to β_o and β_o to ω_o . The OR between the α_2 and ω_o phases (matrices **T**) can be readily obtained by

$$T_{\alpha_2 \rightarrow \omega_o} = B \times C \tag{1}$$

Table 3. The transformation matrices **B** for four ω_o variants from the β_o phase.

Variants	Orientation Relationship	Transformation Matrices B for β_o to ω_o
B1	$(111) \beta_o // (0001) \omega_o$; $[1\bar{1}0] \beta_o // [2\bar{1}\bar{1}0] \omega_o$	$\begin{matrix} \sqrt{2}/2 & -\sqrt{2}/2 & 0 \\ \sqrt{6}/6 & \sqrt{6}/6 & -\sqrt{6}/3 \\ \sqrt{3}/3 & \sqrt{3}/3 & \sqrt{3}/3 \end{matrix}$
B2	$(\bar{1}11) \beta_o // (0001) \omega_o$; $[110] \beta_o // [2\bar{1}\bar{1}0] \omega_o$	$\begin{matrix} \sqrt{2}/2 & \sqrt{2}/2 & 0 \\ -\sqrt{6}/6 & \sqrt{6}/6 & -\sqrt{6}/3 \\ -\sqrt{3}/3 & \sqrt{3}/3 & \sqrt{3}/3 \end{matrix}$
B3	$(1\bar{1}\bar{1}) \beta_o // (0001) \omega_o$; $[110] \beta_o // [2\bar{1}\bar{1}0] \omega_o$	$\begin{matrix} \sqrt{2}/2 & \sqrt{2}/2 & 0 \\ -\sqrt{6}/6 & \sqrt{6}/6 & \sqrt{6}/3 \\ \sqrt{3}/3 & -\sqrt{3}/3 & \sqrt{3}/3 \end{matrix}$
B4	$(11\bar{1}) \beta_o // (0001) \omega_o$; $[1\bar{1}0] \beta_o // [2\bar{1}\bar{1}0] \omega_o$	$\begin{matrix} \sqrt{2}/2 & -\sqrt{2}/2 & 0 \\ -\sqrt{6}/6 & -\sqrt{6}/6 & -\sqrt{6}/3 \\ \sqrt{3}/3 & \sqrt{3}/3 & -\sqrt{3}/3 \end{matrix}$

Table 4. The transformation matrices **C** for six β_o variants from the α_2 phase.

Variants	Orientation Relationship	Transformation Matrices C for α_2 to β_o
C1	$(110) \beta_o // (0001) \alpha_2$; $[\bar{1}\bar{1}1] \beta_o // [21\bar{1}0] \alpha_2$	$\begin{matrix} 1/\sqrt{3} & 1/\sqrt{6} & 1/\sqrt{2} \\ -1/\sqrt{3} & -1/\sqrt{6} & 1/\sqrt{2} \\ 1/\sqrt{3} & -2/\sqrt{6} & 0 \end{matrix} \times L$
C2	$(110) \beta_o // (0001) \alpha_2$; $[\bar{1}\bar{1}1] \beta_o // [21\bar{1}0] \alpha_2$	$\begin{matrix} 1/\sqrt{3} & -1/\sqrt{6} & 1/\sqrt{2} \\ -1/\sqrt{3} & 1/\sqrt{6} & 1/\sqrt{2} \\ -1/\sqrt{3} & -2/\sqrt{6} & 0 \end{matrix} \times L$
C3	$(110) \beta_o // (0001) \alpha_2$; $[\bar{1}\bar{1}1] \beta_o // [\bar{1}2\bar{1}0] \alpha_2$	$\begin{matrix} 1/\sqrt{3} & 1/\sqrt{6} & 1/\sqrt{2} & -1 & 1 & 0 \\ -1/\sqrt{3} & -1/\sqrt{6} & 1/\sqrt{2} & -1 & 0 & 0 \\ 1/\sqrt{3} & -2/\sqrt{6} & 0 & 0 & 0 & 1 \end{matrix} \times L \times$
C4	$(110) \beta_o // (0001) \alpha_2$; $[\bar{1}\bar{1}1] \beta_o // [\bar{1}2\bar{1}0] \alpha_2$	$\begin{matrix} 1/\sqrt{3} & -1/\sqrt{6} & 1/\sqrt{2} & -1 & 1 & 0 \\ -1/\sqrt{3} & 1/\sqrt{6} & 1/\sqrt{2} & -1 & 0 & 0 \\ -1/\sqrt{3} & -2/\sqrt{6} & 0 & 0 & 0 & 1 \end{matrix} \times L \times$
C5	$(110) \beta_o // (0001) \alpha_2$; $[\bar{1}\bar{1}1] \beta_o // [1120] \alpha_2$	$\begin{matrix} 1/\sqrt{3} & 1/\sqrt{6} & 1/\sqrt{2} & 0 & -1 & 0 \\ -1/\sqrt{3} & -1/\sqrt{6} & 1/\sqrt{2} & 1 & -1 & 0 \\ 1/\sqrt{3} & -2/\sqrt{6} & 0 & 0 & 0 & 1 \end{matrix} \times L \times$
C6	$(110) \beta_o // (0001) \alpha_2$; $[\bar{1}\bar{1}1] \beta_o // [1120] \alpha_2$	$\begin{matrix} 1/\sqrt{3} & -1/\sqrt{6} & 1/\sqrt{2} & 0 & -1 & 0 \\ -1/\sqrt{3} & 1/\sqrt{6} & 1/\sqrt{2} & 1 & -1 & 0 \\ -1/\sqrt{3} & -2/\sqrt{6} & 0 & 0 & 0 & 1 \end{matrix} \times L \times$

L is the transformation matrix from the crystallographic coordinate system to the orthogonal coordinate system (see Appendix A). By using Equation (1), the matrices T for α_2 to ω_0 phases are obtained, deriving the arbitrary parallel crystallographic directions between the α_2 and ω_0 phases. According to these results, only four ω_0 variants have good lattice matching and two ORs between the α_2 and ω_0 phases are obtained (see Appendix A.2 for details):

$$\langle 2\bar{1}\bar{1}0 \rangle_{\alpha_2} // \langle 0001 \rangle_{\omega_0}; \{0002\}_{\alpha_2} // \{2\bar{1}\bar{1}0\}_{\omega_0} \text{ORI}$$

$$\langle 2\bar{1}\bar{1}0 \rangle_{\alpha_2} // \langle 2\bar{2}01 \rangle_{\omega_0}; \{0002\}_{\alpha_2} // \{01\bar{1}2\}_{\omega_0} \text{ORII}$$

ORII can be also expressed as $\langle \bar{1}010 \rangle_{\alpha_2} // \langle 2\bar{4}23 \rangle_{\omega_0}; \{0002\}_{\alpha_2} // \{01\bar{1}2\}_{\omega_0}$ by using a superimposed stereographic projection. Thus, both ORs calculated from the transformation matrices are the same as the results obtained by edge-to-edge matching calculation in Ti-45Al-9Nb alloy [10]. According to the results, the selection of OR between the α_2 and ω_0 phases is essentially based on which ω_0 variant has good lattice matching with α_2 phase. It was reported that the misfit between the α_2 and ω_0 phases had a minimum value if ORI was formed [10]. Thus, it is believed that only one ω_0 variant nucleated at the α_2 boundary.

Moreover, according to the EDS results in Table 2, the composition of the ω_0 particle nucleated at the boundary of the α_2 phase is more concentrated in Nb than the β_0 matrix. It is suggested that the ω_0 phase primarily nucleates at the boundary of the α_2 phase and enriches in Nb during growth. Thus, the untransformed area of the periphery of the α_2 phase is depleted in Nb so that the precipitate-free regions are observed.

4.2. Thin γ Plates Precipitated within the α_2 Phase

Because of the misfit matching between the α_2 and ω_0 phases, distortions at the interface are expected. The interplanar spacings of the (0002) α_2 and (11 $\bar{2}$ 0) ω_0 planes measured by HRTEM and SAD software are 0.233 nm and 0.229 nm, respectively. That is a 1.7% mismatch in the interplanar spacing when ORI is formed between the α_2 and ω_0 phases. It means that α_2 phase may have an extra (0002) α_2 plane after successive stacking of 59 pairs of (11 $\bar{2}$ 0) ω_0 and (0002) α_2 planes. The interplanar spacing of (111) γ is 0.232 nm is smaller than that of the (0002) α_2 but larger than (11 $\bar{2}$ 0) ω_0 . Thus, the fine γ plates may relieve the distortion at the interface of the ω_0 and α_2 phases (Figure 4e). It has been reported that the precipitation of γ in α_2 is simply a HCP \rightarrow FCC structure change which can be brought about if $a/6 \langle 10\bar{1}0 \rangle$ type Shockley partials move on alternate basal plane (0001) α_2 planes [31,32]. As mentioned above, an extra (0002) α_2 plane exists after successive stacking of 59 pairs of (11 $\bar{2}$ 0) ω_0 and (0002) α_2 planes. This case may cause the distorted-region separated along the α_2 and ω_0 interface. As a consequence, the sliding of the partial dislocations in the distorted-region can produce separated fine γ plates at certain intervals. Moreover, the interplanar spacing of 59 (0002) α_2 planes is approximate 13.7 nm, which is consistent with the average spacing of the γ laths, which is approximate 12 nm as obtained from Figure 4a.

5. Conclusions

In this work, the precipitation of ω_0 phase in Ti-37.5Al-12.5Nb alloy was examined mainly by TEM. The ORs between different phases were calculated. The main results are summarized as follows:

1. Only one ω_0 variant preferentially nucleates at the α_2 boundaries. This is because the minimum misfit exists at the α_2/ω_0 interface if the OR between these two phases is: $\langle 2\bar{1}\bar{1}0 \rangle_{\alpha_2} // \langle 0001 \rangle_{\omega_0}; \{0002\}_{\alpha_2} // \{2\bar{1}\bar{1}0\}_{\omega_0}$.
2. Precipitate-free regions are observed at the α_2 boundaries. EDS results indicate that the ω_0 precipitates are more concentrated in Nb than β_0 -matrix. The preferred nucleation of the ω_0 variant causes solute depletion surrounding the α_2 plates, which inhibits the nucleation and growth of new ω_0 precipitates in the un-precipitated regions.

3. Thin γ plates precipitate within the α_2 phase. These fine γ plates can relieve the distortion caused by the mismatch at the α_2/ω_0 interface.

Acknowledgments: This research was supported by the National Natural Science Foundation of China under Contract Nos. 51671016, 51601146 and 51271016.

Author Contributions: Lin Song and Junpin Lin conceived and designed the experiments; Teng Ye, Maohua Quan and Jianping He performed the experiments; Teng Ye analyzed the data and wrote the paper.

Conflicts of Interest: The authors declare no conflict of interest.

Appendix A

Because ω_0 and α_2 phases have a hexagonal structure, we can define an orthogonal coordinate system with 'x' axis is $[2\bar{1}\bar{1}0]$ direction, 'y' axis is $[01\bar{1}0]$ direction and 'z' axis is $[0001]$ direction. Then, the transformation matrix from the crystallographic coordinate system to the orthogonal coordinate system can be written as:

$$\mathbf{L} = \begin{pmatrix} a & -a/2 & 0 \\ 0 & \sqrt{3}a/2 & 0 \\ 0 & 0 & c \end{pmatrix}$$

here 'a' and 'c' are lattice parameters.

In order to calculate the ORs between these phases, the indices of the crystallographic direction $[uvw]$ and the crystallographic face (hkl) in the four-index vector must transform into a three-index vector $[u^h v^h w^h]$ and $(h^h k^h l^h)$ in the hexagonal coordinate system, e.g.,

$$u^h = 2u + v; v^h = u + 2v; w^h = w \quad (\text{A1})$$

and

$$h^h = h; k^h = k; l^h = l \quad (\text{A2})$$

Considering a hexagonal structure, the indices of the normal of the crystallographic face $[h^h k^h l^h]$ in the hexagonal coordinate system are: $[2h + k \cdot h + 2k \cdot 3l (a/c)^2 / 2]$. Thus, the index vector $[u' v' w']$ and $[h' k' l']$ in the orthogonal coordinate system can be obtained by $\mathbf{L} \times [u^h v^h w^h]^T$ and $\mathbf{L} \times [h^h k^h l^h]^T$, the relationship between the $[u' v' w']$ and $[uvw]$ is:

$$u' = 3u/2; v' = (u + 2v)\sqrt{3}/2; w' = wc/a \quad (\text{A3})$$

and

$$U = 2u'/3; v = (\sqrt{3}v' - u')/3; t = -(u + v); w = aw'/c \quad (\text{A4})$$

Similarly, the relationship between the $[h' k' l']$ and $[hkl]$ is:

$$h' = \sqrt{3}h; k' = h + 2k; l' = \sqrt{3}l a/c \quad (\text{A5})$$

and

$$H = h' \sqrt{3}/3; k = (k' - h' \sqrt{3}/3)/2; l = cl' \sqrt{3}/3a \quad (\text{A6})$$

Appendix A.1. Transformation Matrices B from β_0 to ω_0

The observed ω_0 phase in high Nb-TiAl alloys can be formed from 'ω-collapse' in the (111) β_0 plane. The OR between ω_0 and β_0 phase can be described as:

$$\langle 110 \rangle_{\beta_0} // \langle \bar{1}\bar{2}10 \rangle_{\omega_0}; \{1\bar{1}\bar{1}\}_{\beta_0} // \{0001\}_{\omega_0} \quad (\text{A7})$$

There are four different crystallographic equivalent $\langle 111 \rangle$ β_o directions in β_o lattice. Thus, four possible ω_o variants exist in the β_o phase with specific ORs between ω_o and β_o phases.

It is convenient to describe the ORs by using '(hkl) [uvw]' matrix, which is written as:

$$\begin{matrix} u & r & h \\ v & s & k \\ w & t & l \end{matrix}$$

All the vectors have been normalized and the orientation matrix **A** of the β_o phase can be written as in Table A1.

Table A1. The orientation matrix **A** of the β_o phase.

Variants	Orientation Relationship	Orientation Matrix A of the β_o Phase		
A1	$(111)\beta_o // (0001)\omega_o$; $[\bar{1}\bar{1}0]\beta_o // [2\bar{1}\bar{1}0]\omega_o$	$1/\sqrt{2}$	$1/\sqrt{6}$	$1/\sqrt{3}$
		$-1/\sqrt{2}$	$1/\sqrt{6}$	$1/\sqrt{3}$
		0	$-2/\sqrt{6}$	$1/\sqrt{3}$
A2	$(\bar{1}\bar{1}1)\beta_o // (0001)\omega_o$; $[1\bar{1}0]\beta_o // [2\bar{1}\bar{1}0]\omega_o$	$1/\sqrt{2}$	$-1/\sqrt{6}$	$-1/\sqrt{3}$
		$1/\sqrt{2}$	$1/\sqrt{6}$	$1/\sqrt{3}$
		0	$-2/\sqrt{6}$	$1/\sqrt{3}$
A3	$(1\bar{1}\bar{1})\beta_o // (0001)\omega_o$; $[1\bar{1}0]\beta_o // [2\bar{1}\bar{1}0]\omega_o$	$1/\sqrt{2}$	$-1/\sqrt{6}$	$1/\sqrt{3}$
		$1/\sqrt{2}$	$1/\sqrt{6}$	$-1/\sqrt{3}$
		0	$2/\sqrt{6}$	$1/\sqrt{3}$
A4	$(1\bar{1}\bar{1})\beta_o // (0001)\omega_o$; $[\bar{1}\bar{1}0]\beta_o // [2\bar{1}\bar{1}0]\omega_o$	$1/\sqrt{2}$	$-1/\sqrt{6}$	$1/\sqrt{3}$
		$-1/\sqrt{2}$	$-1/\sqrt{6}$	$1/\sqrt{3}$
		0	$-2/\sqrt{6}$	$-1/\sqrt{3}$

Thus, the transformation matrices **B** from β_o to ω_o can be obtained by inverse matrices of **A**: $\mathbf{B} = \mathbf{A}^{-1}$, (see Table 3 in the article).

Having noted that the calculated crystal directions of the ω_o phase are described in the orthogonal coordinate, thus, they can be transformed from orthogonal coordinate to crystal coordinate by using the Equation (A4).

Appendix A.2. Transformation Matrices **C** from α_2 to β_o

According to the so-called Burgers OR between the α_2 and β_o phases: $\{110\}\beta_o // (0001)\alpha_2$; $\langle \bar{1}\bar{1}1 \rangle \beta_o // \langle 11\bar{2}0 \rangle \alpha_2$, six β_o variants can form from the α_2 phase (see Table A2). As described above, we can obtain the transformation matrices **C** from α_2 to β_o . However, variants 3 and 4 indicate that the direction of $[\bar{1}\bar{2}\bar{1}0]\alpha_2$ parallels the 'x' axis in the reference coordinate system (which means the crystal coordinate rotates 120° counterclockwise around the $[0001]\alpha_2$). Thus, the transformation matrices should be multiplied by the three-fold rotation matrix under the $[0001]$ axis:

$$\mathbf{R} = \begin{matrix} -1 & 1 & 0 \\ -1 & 0 & 0 \\ 0 & 0 & 1 \end{matrix}$$

Moreover, variant 5 and 6 must be multiplied by the three-fold rotation matrix twice because the crystal coordinate rotates 240° counterclockwise around the $[0001]\alpha_2$. Thus, the transformation matrices **C** from α_2 to β_o can be obtained by **L** and **R**. (see Table 4 in the article).

Then, we can calculate the transformation matrices **T** from α_2 to ω_o , $\mathbf{T} = \mathbf{B} \times \mathbf{C}$. As described above, the calculated crystal directions of the ω_o phase should be transformed from orthogonal coordinate to crystal coordinate by using the Equation (A2).

For instance, when the view direction is $[\bar{2}\bar{1}10]\alpha_2$ and $[000\bar{1}]\alpha_2$, the paralleled crystallographic directions of ω_o are shown in Tables A2 and A3 (Moreover, the parallel crystallographic plane can be obtained from the normal of the crystal face by using Equation (A3)).

Table A2. The paralleled crystallographic directions of different ω_0 variants under $[\bar{2}110] \alpha_2$ direction.

	B1	B2	B3	B4
	[<i>uvtw</i>]	[<i>uvtw</i>]	[<i>uvtw</i>]	[<i>uvtw</i>]
C1	0.54	0	0	0.54
	−0.54	−0.54	0	−0.54
	0	0.54	0	0
	0.277	−0.28	0.83	−0.28
C2	0.54	0	0	0.54
	0	0	−0.54	0
	−0.54	0	0.54	−0.54
	−0.28	−0.83	0.28	0.28
C3	−0.61	0	0	−0.61
	0.11	0.11	0.50	0.11
	0.50	−0.11	−0.50	0.50
	0.20	0.82	−0.42	−0.20
C4	0.06	0	0	0.06
	−0.50	−0.50	0.44	−0.50
	0.44	0.50	−0.44	0.44
	0.48	0.42	0.54	−0.48
C5	0.06	0	0	0.06
	0.44	0.44	−0.50	0.44
	−0.50	−0.44	0.50	−0.50
	−0.48	−0.54	−0.42	0.48
C6	−0.61	0	0	−0.61
	0.50	0.50	0.11	0.50
	0.11	−0.50	−0.11	0.11
	−0.20	0.42	−0.82	0.20

Table A3. The paralleled crystallographic directions of different ω_0 variants under $[0001] \alpha_2$ direction.

	B1	B2	B3	B4
	[<i>uvtw</i>]	[<i>uvtw</i>]	[<i>uvtw</i>]	[<i>uvtw</i>]
C1	0	0.67	0.67	0
	0.33	−0.33	−0.33	−0.33
	−0.33	−0.33	−0.33	0.33
	0.68	0	0	0.68
C2	0	0.67	0.67	0
	0.33	−0.33	−0.33	−0.33
	−0.33	−0.33	−0.33	0.33
	0.68	0	0	0.68
C3	0	0.67	0.67	0
	0.33	−0.33	−0.33	−0.33
	−0.33	−0.33	−0.33	0.33
	0.68	0	0	0.68
C4	0	0.67	0.67	0
	0.33	−0.33	−0.33	−0.33
	−0.33	−0.33	−0.33	0.33
	0.68	0	0	0.68
C5	0	0.67	0.67	0
	0.33	−0.33	−0.33	−0.33
	−0.33	−0.33	−0.33	0.33
	0.68	0	0	0.68
C6	0	0.67	0.67	0
	0.33	−0.33	−0.33	−0.33
	−0.33	−0.33	−0.33	0.33
	0.68	0	0	0.68

References

1. Kim, Y.W. Gamma titanium aluminides: Their status and future. *JOM* **1995**, *47*, 39–42. [[CrossRef](#)]
2. Paul, J.D.H.; Appel, F.; Wagner, R. The compression behaviour of niobium alloyed γ -titanium aluminides. *Acta Mater.* **1998**, *46*, 1075–1085. [[CrossRef](#)]
3. Liu, Z.C.; Lin, J.P.; Li, S.J.; Chen, G.L. Effect of Nb and Al on the microstructures and mechanical properties of high Nb containing TiAl base alloys. *Intermetallics* **2002**, *10*, 653–659. [[CrossRef](#)]
4. Stark, A.; Bartels, A.; Clemens, H.; Schimansky, F.P. On the Formation of Ordered ω -phase in High Nb Containing γ -TiAl Based Alloys. *Adv. Eng. Mater.* **2008**, *10*, 929–934. [[CrossRef](#)]
5. Stark, A.; Oehring, M.; Pyczak, F.; Schreyer, A. In situ observation of various phase transformation paths in Nb-rich TiAl alloys during quenching with different rates. *Adv. Eng. Mater.* **2011**, *13*, 700–704. [[CrossRef](#)]
6. Kainuma, R.; Fujita, Y.; Mitsui, H.; Ohnuma, I.; Ishida, K. Phase equilibria among α (hcp), β (bcc) and γ (L_{10}) phases in Ti–Al base ternary alloys. *Intermetallics* **2000**, *8*, 855–867. [[CrossRef](#)]
7. Chen, G.L.; Xu, X.J.; Teng, Z.K.; Wang, Y.L.; Lin, J.P. Microsegregation in high Nb containing TiAl alloy ingots beyond laboratory scale. *Intermetallics* **2007**, *15*, 625–631. [[CrossRef](#)]
8. Bendersky, L.A.; Boettinger, W.J.; Burton, B.P.; Biancaniello, F.S.; Shoemaker, C.B. The formation of ordered ω -related phases in alloys of composition Ti_4Al_3Nb . *Acta Metall. Mater.* **1990**, *38*, 931–943. [[CrossRef](#)]
9. Song, L.; Zhang, L.Q.; Xu, X.J.; Sun, J.; Lin, J.P. Omega phase in as-cast high-Nb-containing TiAl alloy. *Scr. Mater.* **2013**, *68*, 929–932. [[CrossRef](#)]
10. Song, L.; Xu, X.J.; You, L.; Liang, Y.F.; Wang, Y.L.; Lin, J.P. Ordered α_2 to ω_0 phase transformations in high Nb-containing TiAl alloys. *Acta Mater.* **2015**, *91*, 330–339. [[CrossRef](#)]
11. Schloffer, M.; Rashkova, B.; Schöberl, T.; Schwaighofer, E.; Zhang, Z.; Clemens, H.; Mayer, S. Evolution of the ω_0 phase in a β -stabilized multi-phase TiAl alloy and its effect on hardness. *Acta Mater.* **2014**, *64*, 241–252. [[CrossRef](#)]
12. Huang, Z.W. Ordered ω phases in a 4Zr–4Nb-containing TiAl-based alloy. *Acta Mater.* **2008**, *56*, 1689–1700. [[CrossRef](#)]
13. Jiang, H.; Hu, D.; Wu, X. Thermal stability of the omega phase in Zr-containing TiAl alloys. *J. Alloys Compd.* **2009**, *475*, 134–138. [[CrossRef](#)]
14. Gil, I.; Morris, M.A.; Morris, D.G. The effect of heat treatments on the microstructural stability of the intermetallic Ti–46.5Al–2W–0.5Si. *Intermetallics* **2001**, *9*, 373–385. [[CrossRef](#)]
15. Zhou, L.Z.; Lupinc, V.; Guo, J.T. Microstructural stability of the intermetallic Ti–45Al–2W–0.5Si–0.5B in the 800–980 °C temperature range. *Mater. Sci. Eng. A* **2003**, *354*, 97–105. [[CrossRef](#)]
16. Yin, W.M.; Lupinc, V.; Battezzati, L. Microstructural study of a γ -TiAl based alloy containing W and Si. *Mater. Sci. Eng. A* **1997**, *239–240*, 713–721. [[CrossRef](#)]
17. Huang, Z.W. Thermal stability of Ti–44Al–4Nb–4Hf–0.2Si–1B alloy. *Intermetallics* **2013**, *37*, 11–21. [[CrossRef](#)]
18. Vohra, Y.K.; Sikka, S.K.; Menon, E.S.K.; Krishnan, R. Direct evidence of intermediate state during alpha-omega transformation in Ti–V alloy. *Acta Metall.* **1980**, *28*, 683–685. [[CrossRef](#)]
19. Gupta, S.C.; Sikka, S.K.; Chidambaram, R. On orientation relations between α and ω phases in Zr by texture studies using neutron diffraction method. *Scr. Metall.* **1985**, *19*, 1167–1169. [[CrossRef](#)]
20. Bystrzanowski, S.; Bartels, A.; Stark, A.; Gerling, R.; Schimansky, F.P.; Clemens, H. Evolution of microstructure and texture in Ti–46Al–9Nb sheet material during tensile flow at elevated temperatures. *Intermetallics* **2010**, *18*, 1046–1055. [[CrossRef](#)]
21. Hu, D.; Jiang, H. Martensite in a TiAl alloy quenched from beta phase field. *Intermetallics* **2015**, *56*, 87–95. [[CrossRef](#)]
22. Song, L.; Xu, X.J.; You, L.; Liang, Y.F.; Lin, J.P. Phase transformation and decomposition mechanisms of the $\beta_0(\omega)$ phase in cast high Nb containing TiAl alloy. *J. Alloys Compd.* **2014**, *616*, 483–491. [[CrossRef](#)]
23. Klein, T.; Rashkova, B.; Holec, D.; Clemens, H.; Mayer, S. Silicon distribution and silicide precipitation during annealing in an advanced multi-phase γ -TiAl based alloy. *Acta Mater.* **2016**, *110*, 236–245. [[CrossRef](#)]
24. Ye, T.; Song, L.; Gao, S.B.; Liang, Y.F.; Wang, Y.L.; Lin, J.P. Precipitation behavior of the ω_0 phase in an annealed high Nb–TiAl alloy. *J. Alloys Compd.* **2017**, *701*, 882–891. [[CrossRef](#)]
25. Zhang, L.C.; Cheng, T.T.; Aindow, M. Nucleation of the lamellar decomposition in a Ti–44Al–4Nb–4Zr alloy. *Acta Mater.* **2004**, *52*, 191–197. [[CrossRef](#)]

26. Denquin, A.; Naka, S. Phase transformation mechanisms involved in two-phase TiAl-based alloys—I. Lath structure formation. *Acta Mater.* **1996**, *44*, 343–352. [[CrossRef](#)]
27. Mayer, S.; Petersmann, M.; Fischer, F.D.; Clemens, H.; Waitz, T.; Antretter, T. Experimental and theoretical evidence of displacive martensite in an intermetallic Mo-containing γ -TiAl based alloy. *Acta Mater.* **2016**, *115*, 242–249. [[CrossRef](#)]
28. Wang, S.C.; Aindow, M.; Starink, M.J. Effect of self-accommodation on α/α boundary populations in pure titanium. *Acta Mater.* **2003**, *51*, 2485–2503. [[CrossRef](#)]
29. Liu, H.W.; Luo, C.P.; Yuan, Y.; Liu, J.M.; Liu, Z.G. Interpretation of the morphology and crystallography of precipitate γ_1 -Ti₄Nb₃Al₉ in L1₀-TiAl(Nb)-based intermetallics by invariant line theory. *Intermetallics* **2007**, *15*, 1497–1503. [[CrossRef](#)]
30. Chen, W.; Zhang, J.Y.; Cao, S.; Pan, Y.; Huang, M.D.; Hu, Q.M.; Sun, Q.Y.; Xiao, L.; Sun, J. Strong deformation anisotropies of ω -precipitates and strengthening mechanisms in Ti–10V–2Fe–3Al alloy micropillars: Precipitates shearing vs precipitates disordering. *Acta Mater.* **2016**, *117*, 68–80. [[CrossRef](#)]
31. Zhang, Y.G.; Tichelaar, F.D.; Schapink, F.W.; Xu, Q.; Chen, C.Q. An evidence of stress-induced $\alpha_2 \rightarrow \gamma$ transformation in a γ -TiAl based alloy. *Scr. Metall.* **1995**, *32*, 981–985. [[CrossRef](#)]
32. Wang, J.G.; Zhang, L.C.; Chen, G.L.; Ye, H.Q.; Nieh, T.G. Deformation-induced $\gamma \leftrightarrow \alpha_2$ phase transformation in a hot-forged Ti–45Al–10Nb alloy. *Mater. Sci. Eng. A* **1997**, *239–240*, 287–292. [[CrossRef](#)]



© 2017 by the authors. Licensee MDPI, Basel, Switzerland. This article is an open access article distributed under the terms and conditions of the Creative Commons Attribution (CC BY) license (<http://creativecommons.org/licenses/by/4.0/>).